

Check for updates

# Enhanced Sonodynamic Bacterial Elimination and Wound Healing Therapy Based on Lanthanide Ion Doped Bi<sub>2</sub>WO<sub>6</sub> Nanosheets and Hydrogel Platform

Xinyue Lao, Qiangian Bai, Yifei Zhao, Xingyi Dai, Yuan Liu, Xiao Han, and Jianhua Hao\*

Sonodynamic therapy (SDT) offers tremendous potential in preventing multidrug-resistant bacterial infections, as it is noninvasive and requires no antibiotic dependence, effectively addressing the issue of bacterial resistance. This study implements an ultrasound (US) responsive 2D Bi<sub>2</sub>WO<sub>6</sub> nanosheets (BWO NSs) as sonosensitizers to generate reactive oxygen species (ROS), resulting in sonodynamic broad-spectrum bacterial elimination. Notably, lanthanide Ytterbium ions are introduced (BWO-x%Yb NSs) to boost the generation of ROS, leading to an enhanced antibacterial effect. The RNA sequencing further reveals the underlying antibacterial mechanism, wherein ROS induces lipid oxidation in bacterial cell membranes and deterioration of membrane integrity, ultimately leading to cellular death. In vitro experiments verify that BWO-x%Yb NSs sonosensitizers attain 100% elimination on Methicillin-resistant Staphylococcus aureus (MRSA) and Escherichia coli (E. coli) under US irradiation, demonstrating a broad-spectrum bactericidal ability. Furthermore, to improve the biocompatibility for in vivo SDT, BWO-x%Yb NSs are integrated with hydrogel, serving as a sonosensitizer-hydrogel platform. This platform expedites the healing process of MRSA-infected wounds under ultrasonic stimulation and reduces the wound area by 75% in 10 Days. Therefore, this work highlights the potential of 2D BWO NSs as US-responsive sonosensitizers and a prospective biocompatible sonosensitizer-hydrogel platform for in vivo SDT applications.

X. Lao, Q. Bai, Y. Zhao, X. Dai, Y. Liu, X. Han, J. Hao Department of Applied Physics Faculty of Science The Hong Kong Polytechnic University Hong Kong 999077, China

E-mail: jh.hao@polyu.edu.hk

J. Hao Research Centre for Nanoscience and Nanotechnology The Hong Kong Polytechnic University Hong Kong 999077, China

The ORCID identification number(s) for the author(s) of this article can be found under https://doi.org/10.1002/adfm.202511512

© 2025 The Author(s). Advanced Functional Materials published by Wiley-VCH GmbH. This is an open access article under the terms of the Creative Commons Attribution-NonCommercial-NoDerivs License, which permits use and distribution in any medium, provided the original work is properly cited, the use is non-commercial and no modifications or adaptations are made.

DOI: 10.1002/adfm.202511512

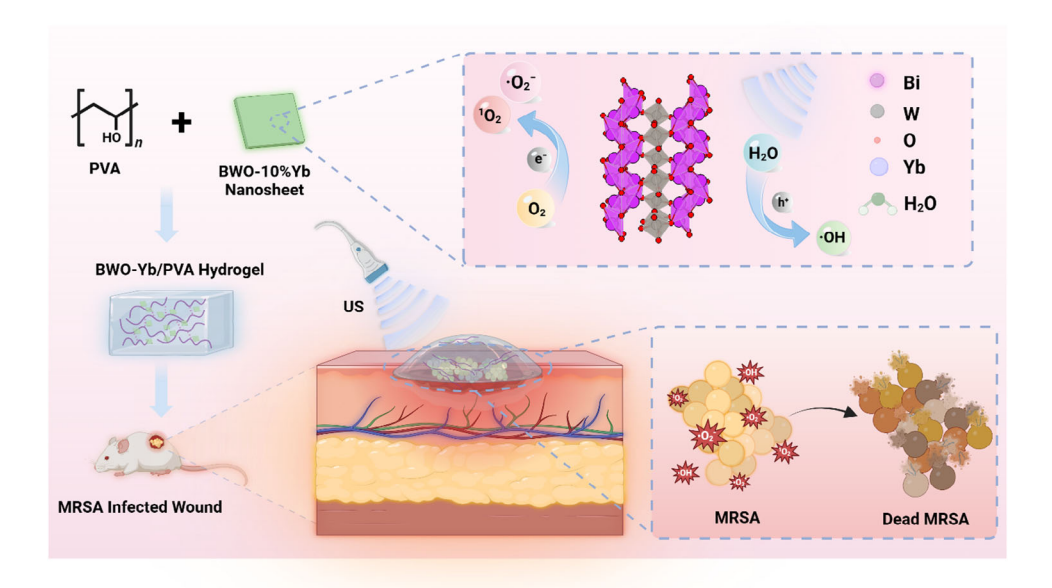
# 1. Introduction

Antimicrobial resistance (AMR) infection is an enormous concern for public health in all regions and at all income levels, leading to millions of deaths worldwide.[1,2] The misuse and excessive use of antimicrobials in clinical treatments for human beings and animals are the primary causes of the formation of drug-resistant pathogens.[3,4] Hence, there is an urgent requirement for novel and inventive approaches to replace the current antibiotic therapy and further address AMR infections. Sonodynamic therapy (SDT) is an innovative approach that employs sonosensitizers to generate highly biotoxic reactive oxygen species (ROS) under ultrasound (US) irradiation to combat drug-resistant bacteria.[5-7] The generated ROS, including singlet oxygen (1O2), hydroxyl radical (·OH), and superoxide anion radical (·O<sub>2</sub>-) are potent antibacterial agents due to their ability to inflict extensive damage to bacterial cellular components and interfere with essential biological processes.<sup>[8,9]</sup> SDT has shown significant promise in clinical therapy for infectious diseases due to its benefits of deep tissue penetration,

low cost, non-invasiveness, and few side effects. [10-12] Nevertheless, SDT is now in its nascent investigation stage and has not yet been extensively used in clinical therapy, mostly owing to the absence of effective sonosensitizers with low toxicity that facilitate the continuous generation of ROS.

Traditional sonosensitizers are developed based on specific types of organic compounds such as hematoporphyrin, phthalocyanines, and xanthenes. Although these organic sonosensitizers have shown effective therapeutic properties, they still suffer from strong hydrophobicity, poor stability, and severe phototoxicity, limiting their potential application in SDT.<sup>[13,14]</sup> In recent times, inorganic piezoelectric nanomaterials such as titanium dioxide (TiO<sub>2</sub>), zinc oxide (ZnO), and barium titanate (BaTiO<sub>3</sub>) have been extensively advanced as promising sonosensitizers in SDT owing to their exceptional physicochemical stability and lower phototoxicity.<sup>[15–18]</sup> When subjected to mechanical vibrations such as US, piezoelectric materials can be polarized to generate a constantly renewed internal electric field, promoting the

16165028.8, D. Downloaded from https://advance.com/inelibrary.vie/s.com/doi/10.1002/drfm.20251151 by HONG KONG POLYTECHNIC UNIVERSITY HU NG HOM, Wiley Online Library on [2609/2025]. See the Terms and Conditions (https://onlinelibrary.vie/scom/terms-and-conditions) on Wiley Online Library for rules of use; O A articles are governed by the applicable Certain Vector Common Statement of the policy of the Common Statement of the Common Sta



Scheme 1. Schematic illustration of Yb-doped Bi<sub>2</sub>WO<sub>6</sub> NSs as sonosensitizer and the BWO-Yb/PVA hydrogel platform for sonodynamic antibacterial therapy.

movement of electrons (e<sup>-</sup>) and holes (h<sup>+</sup>) to migrate toward the opposite surface. [19,20] These e- and h+ are subsequently engaged in redox reactions with nearby oxygen-containing molecules, resulting in the production of ROS. [21] However, the quick recombination of e- and h+ in piezoelectric sonosensitizers triggered by US often leads to a restricted formation of ROS.[22] Approaches have been developed to further improve the formation of ROS of inorganic sonosensitizers, including defect engineering and the construction of heterojunctions.<sup>[23–25]</sup> For example, Mao et al. designed 2D catalytic planar defects within Ti<sub>3</sub>C<sub>2</sub> sheets for highly efficient sonodynamic bactericidal application. [26] The presence of specific planar slip dislocations can yield surface-bound O due to the efficient activation of O2. This results in a significant creation of  ${}^{1}O_{2}$  and a bactericidal capacity of 99.72%  $\pm$  0.03% when subject to US stimulation. Despite significant advancements in the structural engineering of inorganic sonosensitizers, substantial opportunities remain to enhance their ROS generation effectiveness for achieving highly efficient SDT.

The 2D bismuth-based nanomaterials, including Aurivilliusstructured bismuth tungstate (Bi<sub>2</sub>WO<sub>6</sub>), bismuth molybdate (Bi<sub>2</sub>MoO<sub>6</sub>), Sillén-structured BiOX (X = Cl, Br, I), have garnered significant interest in enhanced SDT or synergetic therapies due to their interleaved layered structures, which facilitate the formation of internal electric field and promote effective charge separation. [27,28] Bi<sub>2</sub>WO<sub>6</sub> nanosheets (NSs) with alternating perovskite-like  $(WO_4)^{2-}$  and fluorite-like  $(Bi_2O_2)^{2+}$  blocks enabled exceptional photocatalytic.[29,30] In addition, it has been reported that the orthorhombic structured Bi<sub>2</sub>WO<sub>6</sub> (BWO) with space group *P21ab* exhibits superior piezoelectric response.<sup>[31,32]</sup> Therefore, BWO NSs are promising as sonosensitizers for sonodynamic antibacterial applications.

In this work, orthorhombic-structured BWO NSs were employed as sonosensitizers for sonodynamic antibacterial applications. In addition, Yb ions were introduced into the BWO nanostructure to narrow the bandgap of BWO NSs and enhance the bonding interaction between BWO NSs and H2O, resulting in an increased generation of ROS under US stimulation, achieving effective antibacterial treatment and enhanced SDT performance. Then the DFT simulation further identifies that the Yb in BWO NSs boosted the ROS generation effectiveness. Furthermore, the RNA sequencing transcriptome analysis was conducted to acquire a comprehension of the biological mechanism of sonodynamic antimicrobial activities. Nevertheless, the biocompatibility of inorganic sonosensitizers remains a considerable problem, necessitating surface changes for in vivo sonodynamic therapeutic applications. [26,33-35] Therefore, hydrogels were introduced to load the sonosensitizer owing to their high biocompatibility, large loading capacity, and mechanical properties similar to soft tissue.[36,37] Herein, the as-prepared Yb-doped BWO NSs were combined with PVA hydrogel to improve biocompatibility for further in vivo antibacterial wound healing applications. Consequently, the sonosensitizer-loaded PVA hydrogel significantly accelerated the drug-resistant bacteria-infected wound healing process under US irradiation (Scheme 1). The results in this study demonstrate that the novel Yb-doped BWO NSs sonosensitizer would enable enhanced sonodynamic bacteria elimination and provide a prospective sonosensitizer-hydrogel platform for extremely effective in vivo sonodynamic antibacterial therapy.

#### 2. Results and Discussion

#### 2.1. Synthesis and Characterization of Yb-Doped Bi<sub>2</sub>WO<sub>6</sub> Nanosheets

The 2D Bi<sub>2</sub>WO<sub>6</sub> NSs and Yb-doped Bi<sub>2</sub>WO<sub>6</sub>-x%Yb NSs were synthesized through a simple hydrothermal method. [38] As illustrated in Figure 1a, BWO-x%Yb NSs with different Yb doping concentrations (1%, 2%, 5%, 10%, and 20%) were fabricated by varying the initial feeding ratio of Yb(NO<sub>3</sub>)<sub>3</sub>, named as

16163028, 0, Downloaded from https://advanced.onlinelibrary.wiley.com/doi/10.1002/adfm.202511512 by HONG KONG POLYTECHNIC UNIVERSITY HUNG HOM, Wiley Online Library on [26/09/2025]. See the Terms and Conditions (https://onlinelibrary.

and-conditions) on Wiley Online Library for rules of use; OA articles are governed by the applicable Creative Commons License

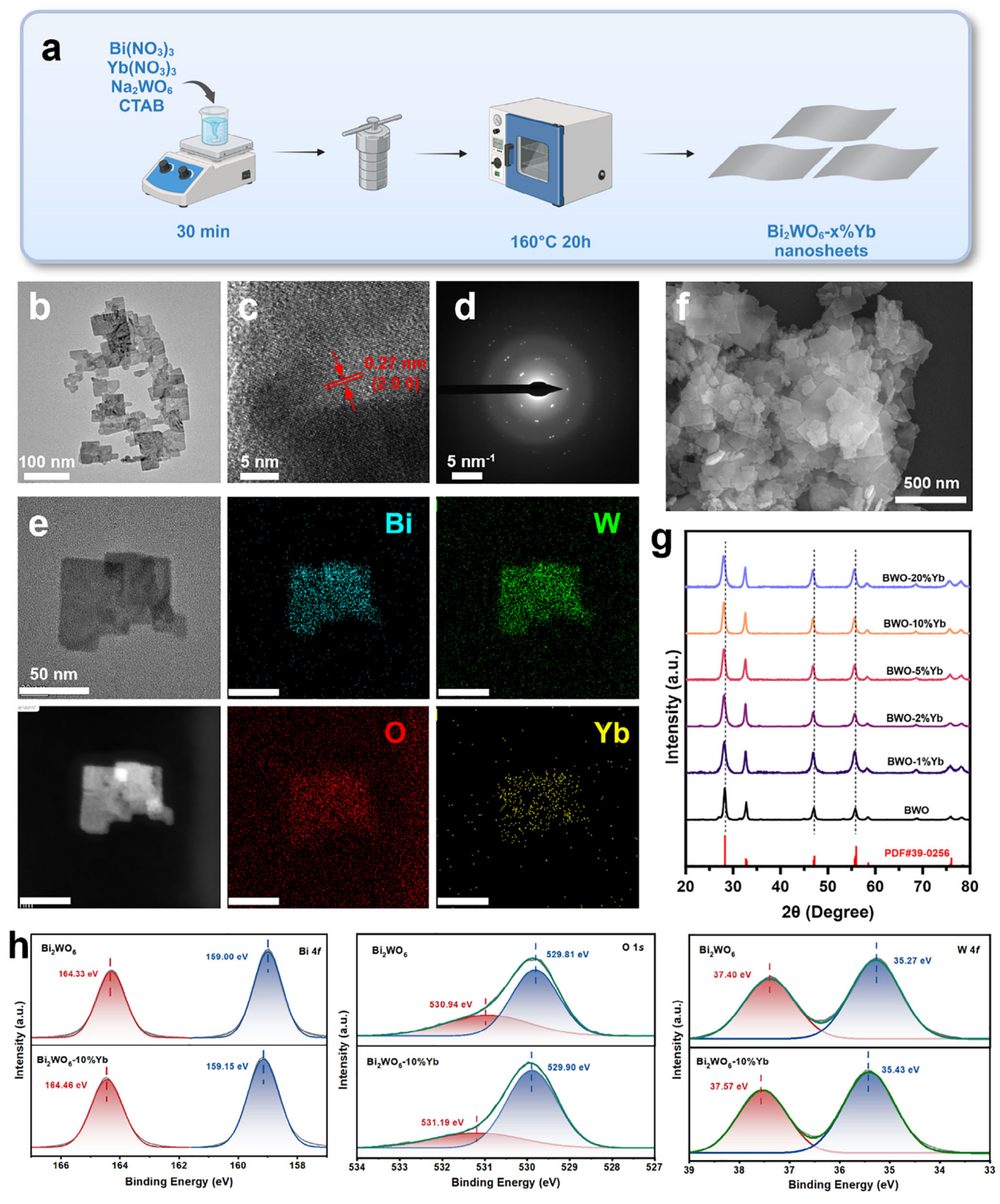


**Figure 1.** a) Illustration of the synthesis route of BWO and BWO-x%Yb NSs. b) TEM image and c) HRTEM image of BWO-10%Yb NSs. d) Selected area electron diffraction (SAED) pattern of BWO-10%Yb NSs. e) Element mapping images (Bi, W, O, and Yb) of BWO-10%Yb NSs, scale bar: 50 nm. f) SEM of BWO-10%Yb NSs. g) XRD spectrum of BWO and BWO-x%Yb NSs. h) High-resolution XPS spectra of Bi 2*p*, O 1s, and W 4*f* of BWO and BWO-10%Yb NSs.





www.afm-journal.de

BWO-1%Yb, BWO-2%Yb, BWO-5%Yb, BWO-10%Yb, and BWO-20%Yb, respectively. Since the efficacy of SDT highly depends on the generation of ROS to disrupt bacterial membranes. The chemical composition and structural properties of the sonosensitizer are crucial fundamentals for the later verification of ROS generation performance and DFT calculation. Therefore, the morphology, structures and chemical composition of the BWO and Yb-doped BWO NSs (BWO-10%Yb NSs for representation) were examined to confirm the successful incorporation of Yb into the BWO nanosheet structure without altering its layered perovskite configuration. The transmission electron microscopy (TEM) image demonstrates that the prepared BWO (Figure S1, Supporting Information) and BWO-10%Yb NSs (Figure 1b) both possess a consistent nanosheet morphology with a dimension ranging from 100 to 200 nm. The high-resolution TEM (HRTEM) image of the BWO-10%Yb NSs displays a continuous lattice fringe, proving conclusive confirmation of its single crystalline structure, as shown in Figure 1c. The determined lattice distance is  $\approx$ 0.27 nm, corresponding to the (200) planes of the orthorhombic phase of BWO crystal. In addition, the single-crystalline nature of BWO-10%Yb nanosheets was further verified by the selected area electron diffraction (SAED) pattern (Figure 1d). The element mapping images in Figure 1e also confirmed that Bi, W, O, and Yb were evenly distributed throughout the BWO-10%Yb NSs, providing evidence of the successful doping of Yb in BWO nanostructure. The scanning electron microscopy (SEM) image revealed that BWO-10%Yb NSs (Figure 1f; Figure S2, Supporting Information) exhibited a characteristic 2D nanosheet structure, with the majority of the nanosheets displaying rectangular shapes. Moreover, X-ray diffraction (XRD) analysis in Figure 1g showed that all the characteristic diffraction patterns were well consistent with the orthorhombic phase of Bi<sub>2</sub>WO<sub>6</sub> (PDF#39-0256). The peaks of the BWO-x%Yb NSs were slightly shifted to a smaller angle when compared to the undoped BWO NSs. The shift grew more pronounced with increasing Yb doping concentration, suggesting that the addition of Yb to the BWO lattice raised the lattice constant since the atomic radius of Yb is larger than that of Bi. The surface element chemical state of BWO and BWO-10%Yb NSs was analyzed by X-ray photoelectron spectroscopy (XPS). The survey XPS spectra of BWO-10%Yb NSs confirmed the existence of Bi, W, O, and Yb elements (Figure S3, Supporting Information), the peak at 188.18 eV in the inset of Figure \$3 (Supporting Information) was assigned to the binding energy of Yb 4d. The high-resolution XPS spectra of Bi 4f, O 1s, and W 4f with fitted curves are displayed in Figure 1h. The XPS high-resolution spectra of O 1s in Bi<sub>2</sub>WO<sub>6</sub> NS exhibited two major peaks at 529.81 and 530.94 eV, attributed to the lattice oxygen and bridging hydroxyls, respectively.<sup>[38]</sup> Besides, the peaks of Bi 4f (Bi  $4f_{7/2}$  159.15 eV and Bi  $4f_{5/2}$  164.46 eV) and W 4f (W  $4f_{5/2}$ 35.43 eV and W  $4f_{7/2}$  37.57 eV) of BWO-10%Yb NS slightly shifted to higher energy compared with pure Bi<sub>2</sub>WO<sub>6</sub> NS, because Yb might change the chemical environment of Bi and W in Bi<sub>2</sub>WO<sub>6</sub> NS. The oxygen defect was further investigated using electron spin resonance (ESR) spectroscopy. As displayed in Figure S4 (Supporting Information), both BWO and BWO-10%Yb NSs are distinguished by their symmetrical ESR signal at g = 2.003, indicating electron trapping at OVs. The ESR results demonstrate that both BWO and BWO-x%Yb NSs possess few OVs, indicating that the change of ROS performance may be caused by a nar-

rowed band gap or absorption of  $\rm H_2O$  instead of generating more OVs

# 2.2. The ROS Generation Performance and Mechanism of the Sonosensitizers

In SDT, ROS are generated when sonosensitizers are activated by ultrasound. These ROS are highly reactive and can cause significant oxidative damage to bacterial cells. ROS can damage bacterial cell membranes, proteins, and DNA, leading to cell lysis and death.[8] This is particularly effective against bacteria that are resistant to conventional antibiotics. Efficient ROS generation leads to enhanced antibacterial activity. The catalytic activities of BWO and BWO-x%Yb NSs as sonosensitizers for generating ROS under US irradiation (1.5 W cm<sup>-2</sup>, 50% duty cycle, 1 MHz) were first examined using 1,3-Diphenylisobenzofuran (DPBF) as singlet oxygen (<sup>1</sup>O<sub>2</sub>) probe. <sup>[39]</sup> The synthesized BWO-x%Yb was uniformly dispersed in DI water to form a white emulsion and examined with 20 µM DPBF. It was anticipated that the presence of <sup>1</sup>O<sub>2</sub> would result in a reduction in the absorption of DPBF at 420 nm. As shown in Figure 2a,b, the groups exposed to US irradiation exhibited a more pronounced and rapid decline in the absorption at 420 nm compared to the groups that were not exposed to the US, suggesting the production of <sup>1</sup>O<sub>2</sub> occurred at a higher rate in the US-triggered groups. Significantly, BWO-10%Yb NSs demonstrate the most rapid decline, with a fall of more than 50% within 10 min of ultrasound irradiation (Figure 2b), which indicates that BWO-10%Yb NSs possess a greater capacity to generate <sup>1</sup>O<sub>2</sub> compared to BWO and other BWO-x%Yb NSs. In contrast, other BWO-x%Yb NSs demonstrate a similar decline (<20%) upon US irradiation. Therefore, the doping of Yb at a concentration of 10% can significantly enhance the SDT performance of the sonosensitizer. Subsequently, the DPBF probe was also employed to investigate the optimized concentration of BWO-10%Yb NSs for generating ROS under US irradiation. The concentrations of BWO-10%Yb NSs at 200 µg mL<sup>-1</sup>, 500 µg mL<sup>-1</sup>, 1 mg mL<sup>-1</sup>, and 2 mg mL<sup>-1</sup> are compared here. Figure 2c demonstrates that a significant reduction in absorption at 420 nm occurred after 10 min of US irradiation at the BWO-10%Yb NSs concentration of 500 μg mL<sup>-1</sup>, indicating that the BWO-10%Yb NSs produced the highest amount of <sup>1</sup>O<sub>2</sub> at this particular concentration. Therefore, 500 µg mL<sup>-1</sup> of BWO-10%Yb NSs was used as the sonosensitizer for further sonodynamic antibacterial investigations.

Furthermore, the generation of the specific ROS, ◆OH, ¹O₂, and O₂⁻, was confirmed by ESR spectroscopy (Figure 2d–f) using 2,2,6,6-tetramethyl-4-piperidone (TEMP) and 5,5-Dimethyl-1-Pyrroline-N-Oxide (DMPO) as spin trapping agents. The results revealed that BWO-10%Yb NSs demonstrated a robust ◆OH signal and slightly lower signals for ¹O₂ and O₂⁻ when exposed to US irradiation, while no signal was detected without US irradiation. indicating excellent sonodynamic performance for generating ROS. Therefore, the above-mentioned findings demonstrate the solid capacity of BWO-10%Yb NSs as a sonosensitizer to sufficiently generate ROS when exposed to US irradiation. This advancement addresses the longstanding challenge of developing inorganic sonosensitizers that exhibit high efficiency in ROS production. Consequently, BWO-10%Yb NSs demonstrate

16163028, 0, Downloaded from https://advanced.onlinelibrary.wiley.com/doi/10.1002/adfm.202511512 by HONG KONG POLYTECHNIC UNIVERSITY HUNG HOM, Wiley Online Library on [26/09/2025]. See the Terms and Conditions (https://onlinelibrary.

and-conditions) on Wiley Online Library for rules of use; OA articles are governed by the applicable Creative Commons License

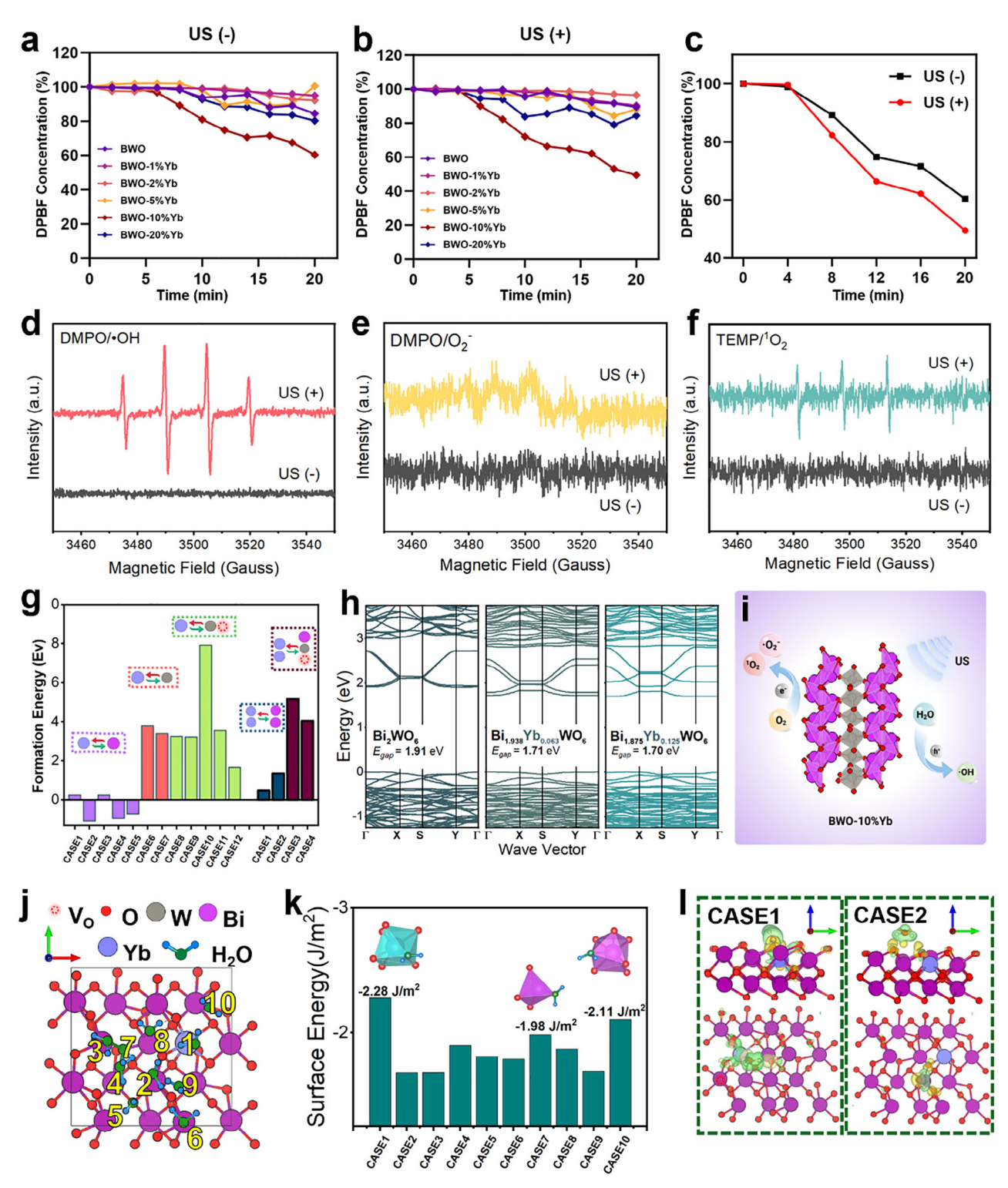


Figure 2. Absorption intensity changes of DPBF in BWO-x%Yb NSs a) without and b) with the US irradiation. c) Absorption intensity of DPBF with different concentrations of BWO-10%Yb NSs under the US irradiation. ESR spectra of d)  $\bullet$ OH and e)  $\bullet$ O<sub>2</sub><sup>-</sup> trapped by DMPO, f)  $^1$ O<sub>2</sub> trapped by TEMP of BWO-10%Yb NSs. g) Defect formation energy of different Yb-doping configurations in BWO, the involved ion substitution in each calculation is marked. h) Evolution of electronic band structure upon Yb doping. i) Schematic illustration of the generation of ROS by US-triggered BWO-10%Yb NSs. j) Crystal structure of BWO-Yb NSs and the surface H<sub>2</sub>O absorption sites, viewing along the c axis. k) The surface energy of H<sub>2</sub>O absorbed at different surface sites. l) The calculated CCD diagram of H<sub>2</sub>O absorbed on surface sites 1 and 2 of BWO-Yb indicates in Figure 2j. The yellow and green regions depict the electron accumulation and depletion, respectively.





www.afm-journal.de

significant potential for sonodynamic therapy, by serving as a novel sonosensitizer to combat bacteria that have developed resistance to traditional antibiotics.

In order to obtain physical insights into the enhanced SDT performance of BWO NCs upon Yb-doping, density functional theory (DFT) simulation was then carried out (See Supporting Information for details). First, the preferential occupation of Yb into the BWO lattice is investigated by comparing the defect formation energy. Based on a 2 × 2 × 1 supercell of BWO, in total 16 cases of different Yb-doping configurations were considered (Figure S5, Supporting Information), such as Yb incorporating Bi site or Yb substituting a W atom and generating one VO for charge compensation. As compared in Figure 2g, all the cases agree on an energetically preferred Yb-Bi substitution despite the different doping concentrations. Following the doping configuration with the lowest formation energy, the impact of Yb dopants on the electronic properties of BWO was then investigated. As shown in Figure 2h, it is found that the introduction of Yb can effectively reduce the bandgap of pristine BWO (1.91 eV) to a lower value (1.71 eV). It is argued that appropriately low electronic bandgap value can facilitate the SDT efficiency.<sup>[40]</sup> Further increasing the Yb-doping concentration (two Yb replacing two Bi atoms, yielding a 12.5 at.% doping concentration) causes a little reduction in bandgap value (1.70 eV), yet it prompts additional band splitting within the conduction band (CB). The broadening of the CB may potentially facilitate the absorption of a broader energy spectrum from the US excitation source, leading to improved SDT efficiency as schematically illustrated in Figure 2i.

Furthermore, we discovered that the introduction of Yb is beneficial to the SDT process in terms of a more selective H<sub>2</sub>O absorption. The preliminary calculation shows that Yb tends to be incorporated at the surficial Bi-O layers of the BWO NSs and with relatively large local distortion, which agrees with similar reports in lanthanide-doped oxide nanosheets. [41] The surface energies (γ) of H<sub>2</sub>O absorbed on different surface sites (schematically shown in Figure 2j and Figure S6, Supporting Information) of BWO NS were then calculated and compared.[42] As summarized in Figure 2k, the lowest  $\gamma$  value was obtained from the case where H<sub>2</sub>O is intentionally absorbed near the surface Yb site. The charge density diagram (CCD) of H<sub>2</sub>O absorption can provide a closer insight into the enhanced bonding interaction between the H<sub>2</sub>O absorbance and Yb sites, rather than other Bi counterparts. Four representative absorption schemes were selected, and the corresponding CCD figures are shown in Figures 21 and S7 (Supporting Information). Compared to the other cases, there is a stronger electronic interaction between the surface Yb site and the absorbed water molecules for CASE1, which is characterized by a more pronounced charge redistribution around the Yb site and water molecules. Such stronger interaction not only facilitates water absorption but also primes the system for subsequent SDT reactions via electron transfer. The absorbed water molecules can readily participate in redox reactions, serving as reactants converted into ROS. In summary, the introduction of Yb theoretically induces a narrowed bandgap and widened CB of BWO, as well as a more selective and effective H<sub>2</sub>O absorption onto the BWO NS surface. All the factors collectively contribute to an enhanced SDT performance as demonstrated by the following experimental characterizations.

Adv. Funct. Mater. 2025, 2511512

#### 2.3. In Vitro Sonodynamic Bactericidal Performance

<sup>1</sup>O<sub>2</sub>, with its longer diffusion range, can affect a broader area within the bacterial cell, potentially leading to more widespread damage. In contrast, •OH acts very locally, causing intense damage at specific sites.<sup>[43]</sup> While <sup>1</sup>O<sub>2</sub> initiates broader oxidative stress, •OH can cause acute damage, leading to rapid bacterial cell death. Therefore, the combination of 10, and •OH can be particularly effective in antibacterial SDT. Since we have demonstrated that BWO-10%Yb NSs have the ability to generate high amount of <sup>1</sup>O<sub>2</sub> and •OH upon US irradiation, we then evaluated the anti-bactericidal performance of BWO-10%Yb NSs in vitro. The sonodynamic bactericidal performance was determined by counting the bacterial colony-forming units (CFU) spread on the LB agar plate after different treatments. The initial concentration of bacteria suspensions in each group was 10<sup>6</sup> CFU mL<sup>-1</sup>, and the suspensions after different treatments were diluted in the same multiple before being spread on the LB agar plate. The US applied to all the in vitro antimicrobial experiments is 1.5 W cm<sup>-2</sup>, 50% duty cycle, 1 MHz. The sonodynamic bactericidal performance of BWO NSs and BWO-10%Yb NSs as sonosensitizers was first examined using the time-dependent plate counting assay, with US irradiation performed for 0, 2, 4, 6, 8, and 10 min, respectively (Figure S8a, Supporting Information). The number of MRSA cells on the plate before exposure to US (0 min) is similar in both BWO NS and BWO-10%Yb NS groups, suggesting that the initial concentration of MRSA cells remains comparable in both groups. After being exposed to 6 min of US irradiation, the group of BWO-10%Yb NSs as sonosensitizer achieved a 100% antibacterial rate against MRSA, while the BWO NSs as sonosensitizer required 10 min in comparison (Figure S8b, Supporting Information). This result provides evidence that Yb-doped BWO NSs demonstrate a superior sonodynamic bactericidal performance compared with BWO NSs owing to the greater production of ROS. Subsequently, the broad-spectrum sonodynamic bactericidal performance of BWO-10%Yb NSs as sonosensitizer was examined on gram-positive and gram-negative bacteria. Herein, the Methicillin-resistant Staphylococcus aureus (MRSA) was chosen as the representative gram-positive bacteria, and Escherichia coli (E. coli) was the representative gram-negative bacteria model, respectively. The gram-negative bacteria have an additional lipid bilayer containing lipopolysaccharides (LPS), which act as a barrier to many substances, including antibiotics and ROS. The lack of an outer membrane for gram-positive bacteria makes them more susceptible to ROS penetration, while the outer membrane of gram-negative bacteria acts as a formidable barrier to ROS penetration.[44] Therefore, the US irradiation time for grampositive MRSA is 5 min, whereas for gram-negative E. coli is 10 min, owing to their distinct structures. Figure 3a demonstrates that there were no discernible bactericidal effects in any of the control groups (Control US(-), Control US(+), and BWO-10%Yb US(-)), as evidenced by the presence of visible colonies of MRSA and E. coli cells on the LB agar plate. Nevertheless, both MRSA and E. coli were eliminated in the groups subjected to BWO-10%Yb NSs and US (BWO-10%Yb US(+)). The colonies of MRSA and E. coli remained constant at 106 CFU/mL in the control groups (p > 0.05) and reduced to 0 CFU/mL in the treatment group with the presence of BWO-10%Yb NSs and US (Figure 3b,c; Figure S9, Supporting Information). The results

16163028, 0, Downloaded from https://advanced.onlinelibrary.wiley.com/doi/10.1002/adfm.202511512 by HONG KONG POLYTECHNIC UNIVERSITY HU NG HOM, Wiley Online Library on [26.09/2025]. See the Terms

onditions) on Wiley Online Library for rules of use; OA articles are governed by the applicable Creative Commons License

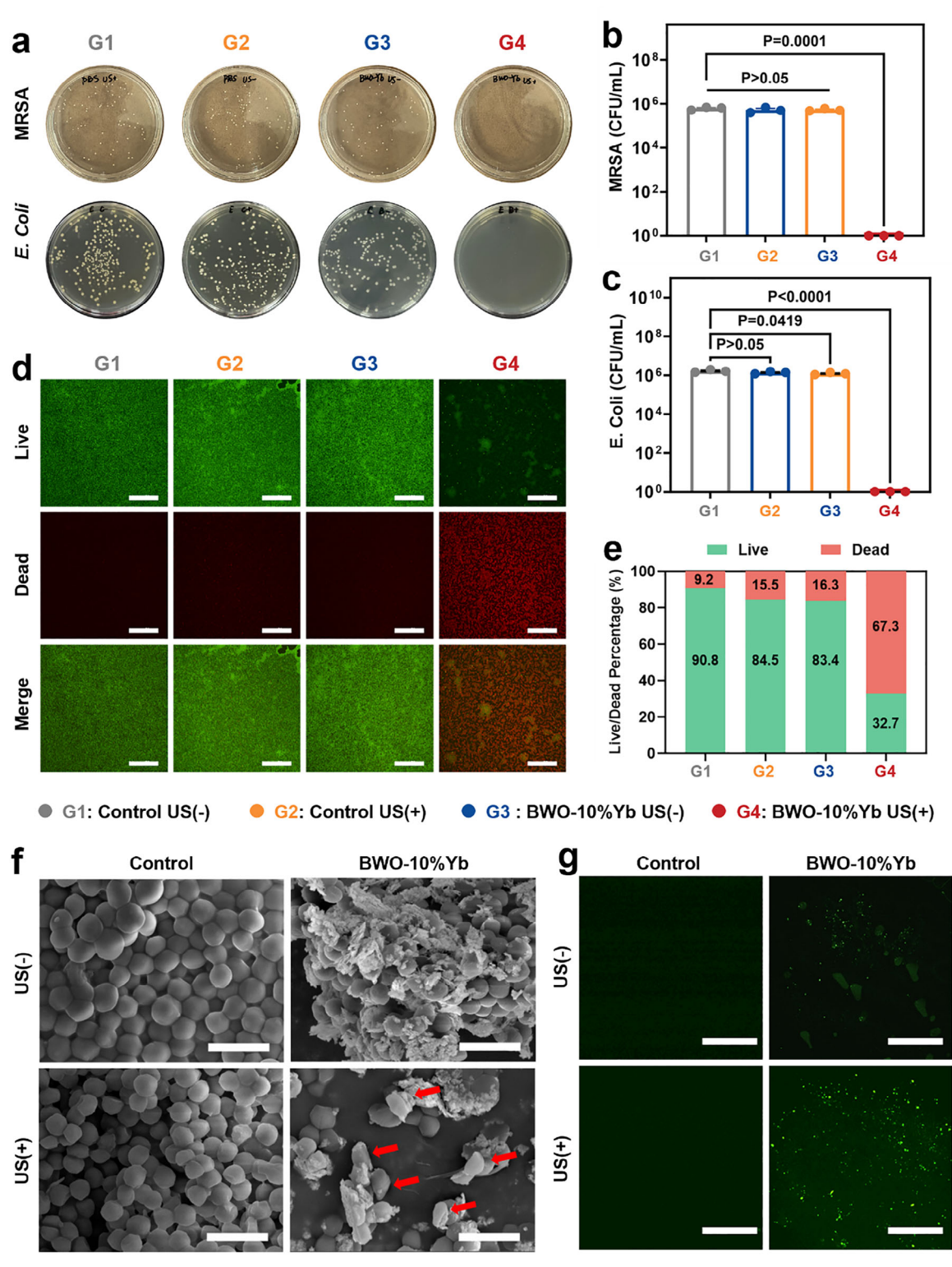


Figure 3. Sonodynamic bactericidal performance of BWO-10%Yb NSs as sonosensitizers. a) Pictures of MRSA (first row) and *E. coli* (second row) colonies coated on LB-agar plates after different treatments (G1: Control US(-), G2: Control US(+), G3: BWO-10%Yb US(-), G4: BWO-10%Yb US(+)). Corresponding bacterial colonies of b) MRSA and c) *E. coli* in different groups (n=3). The error bars indicate mean  $\pm$  SEM. The statistical analysis was performed using one-way ANOVA with Dunnett's multiple-comparisons test. d) Fluorescent images of live (green) and dead (red) MRSA cells after different treatments. Scale bars: 50  $\mu$ m. e) Corresponding quantitative analysis of live/dead fluorescent intensity. f) SEM images of MRSA cells after different treatments. Scale bars: 2  $\mu$ m. Red arrows denote morphological damage in MRSA cells. g) The fluorescence image of MRSA stained with DCFH-DA fluorescent probe in different treatment groups. Scale bars: 500  $\mu$ m.



www.afm-journal.de

confirmed the exceptional antibacterial efficacy of BWO-10%Yb NSs as a sonosensitizer in treating both gram-positive and gramnegative bacteria.

Then the antibacterial efficacy of BWO-10%Yb NSs under US irradiation was evaluated by conducting live/dead dual-color fluorescent staining and observed through a confocal laser scanning microscope (CLSM) (Figure 3d). Most of the MRSA cells treated with PBS, US only, and BWO-10%Yb NSs only were able to remain alive (green), with quantitative analysis indicating survival rates of 90.8%, 84.5%, and 83.4%, respectively (Figure 3e). On the contrary, the majority of MRSA cells exposed to BWO-10%Yb NSs and US were nonviable (red), with a significantly reduced survival rate of merely 32.7%. These findings were consistent with the results obtained from the spread plate counting analysis.

In addition, the MRSA cells in different groups were fixed after treatments, and their morphology was investigated with SEM (Figure 3f). The morphology of MRSA in the control group treated without US (Control US(-)) possessed a typical spherical morphology and smooth appearance. While in the group treated with US only (Control US(+)), MRSA cells remained undamaged but processed a tiny indentation on the surface, indicating minimal mechanical damage caused by US irradiation. Similarly, the MRSA bacteria treated solely with BWO-10%Yb NSs (BWO-10%Yb US(-)) preserve their structural integrity, with BWO-10%Yb NSs adhering to the cell surface. As for the MRSA treated with BWO-10%Yb NSs and US (BWO-10%Yb US(+)), the bacteria exhibited a far more pronounced wrinkling and concave shape, and some membranes were entirely fragmented (red arrows in Figure 3f). The high-resolution SEM images of MRSA treated with BWO-10%Yb NSs and US were also captured and displayed in Figure S10 (Supporting Information), clearly demonstrating the broken cell membrane with BWO-10%Yb NSs attached to the cell surface. Moreover, a strong binding affinity of the BWO-10%Yb to the bacterial cell wall was observed, which may enhance the sonodynamic antibacterial efficacy.

To further verify the ROS-induced bacterial mortality, the ROS generation quantification was evaluated in vitro by a ROS detection assay, 2',7'-Dichlorodihydrofluorescein diacetate (DCFH-DA). In a typical ROS detection assay, DCFH-DA was loaded into living MRSA cells and hydrolyzed by intracellular esterase to produce DCFH. After subjecting MRSA cells to different treatments, the ROS can oxidize non-fluorescent DCFH to fluorescent 2'7'-dichlorofluorescein (DCF). The fluorescent intensity of DCF serves as an indicator of ROS level. From Figure 3g, the MRSA cells in groups treated with PBS, US only, and BWO-10%Yb NSs exhibit feeble fluorescent signals. In contrast, the MRSA cells in the group treated with BWO-10%Yb NSs and US exhibited an intense fluorescent signal of DCF, demonstrating the high ROS generation efficiency of BWO-10%Yb NSs under US irradiation. Therefore, the SEM and ROS detection results conclusively demonstrated that the excessive ROS generated by the BWO-10%Yb NSs sonosensitizer under US irradiation triggered the disruption of bacterial membrane and led to cellular death. Moreover, the damaged bacterial cell walls and membranes make bacteria more susceptible to antibiotics, which can lower the required dose of antibiotics and reduce the risk of resistance development. Consequently, BWO-10%Yb NSs serve as promising sonosensitizers for US-triggered bacterial elimination or combine with antibiotics for antibiotic-resistant infection treatment.

#### 2.4. RNA Sequencing Transcriptome Analysis

The RNA sequencing transcriptome analysis was conducted with MRSA treated with PBS (Control) and BWO-10%Yb NSs + US to acquire further understanding of the biological mechanism of the sonodynamic antimicrobial activities (n = 3 biological replicates). Figure S11 (Supporting Information) reveals that out of 2470 genes that were co-expressed in the control and BWO-10%Yb NSs + US groups, 24 genes were present only in the control group, and 98 genes were expressed mainly in the treatment group, revealing that the BWO-10%Yb NSs + US significantly affected gene expression compared to the control group. In addition, the Volcano Plot in Figure 4a demonstrates the statistical significance (|log, FoldChange| > 1, p-adjust < 0.05) in gene expression levels in the two groups. A total of 245 differentially expressed genes (DEGs) were identified in the control and BWO-10%Yb NSs + US groups, consisting of 130 up-regulated genes and 115 down-regulated genes, indicating a rather substantial response in the BWO-10%Yb NSs + US group. Genes with similar functions or close relationships were clustered into various categories to better comprehend and classify these DEGs. The gene expression patterns of the BWO-10%Yb NSs + US-treated group were then compared with those of the control group in these categories. The results presented in Figure S12 (Supporting Information) demonstrate that the BWO-10%Yb NSs + UStreated group differs considerably from the control group in the gene expression patterns of various categories. To determine the specific functions of these DEGs, gene ontology (GO) term classification analysis was carried out across biological processes (BP), cellular components (CC), and molecular function (MF) terms (Figure 4b). DEGs associated with "catalytic activity, acting on a nucleic acid", "oxidoreductase activity", "catalytic activity, acting on a protein", and "catabolic process" GO terms were observed, which are related to oxidative stress induced by ROS. The GO terms "transmembrane transporter activity", "membrane", and "transmembrane transport" indicate that the ROS may damage the integrity of the bacterial membrane. The DEGs are mostly related to the antibacterial mechanism of BWO-10%Yb NSs. which generate ROS under ultrasound stimulation, leading to the degradation of bacterial genetic material and cell membranes.

Then the enrichment analysis of the Kyoto Encyclopedia of Genes and Genomes (KEGG) pathways was conducted, and the top 20 KEGG pathways of the up-regulated and down-regulated DEGs are depicted in Figure 4c. The upregulated DEGs enriched in the "pyrimidine metabolism" pathway, which is crucial for synthesizing nucleotides, suggest that ROS may induce nucleic acid degradation and lead to increased DNA replication. [45] In addition, the upregulated DEGs were also enriched in "fatty acid degradation" pathway. This pathway breaks down fatty acids into acetyl-CoA units, which can enter the tricarboxylic acid (TCA) cycle to produce ATP. Upregulation of genes associated with TCA cycle is also observed (Figure S13, Supporting Information). While this can provide energy, excessive degradation can deplete membrane lipid components, compromising membrane integrity and function. Downregulated DEGs are

16163028, 0, Downloaded from https://advanced.onlinelibrary.wiley.com/doi/10.1002/adfm.202511512 by HONG KONG POLYTECHNIC UNIVERSITY HU NG HOM, Wiley Online Library on [26.09/2025]. See the Terms

and Conditions (https://onlinelibrary

onditions) on Wiley Online Library for rules of use; OA articles are governed by the applicable Creative Commons License

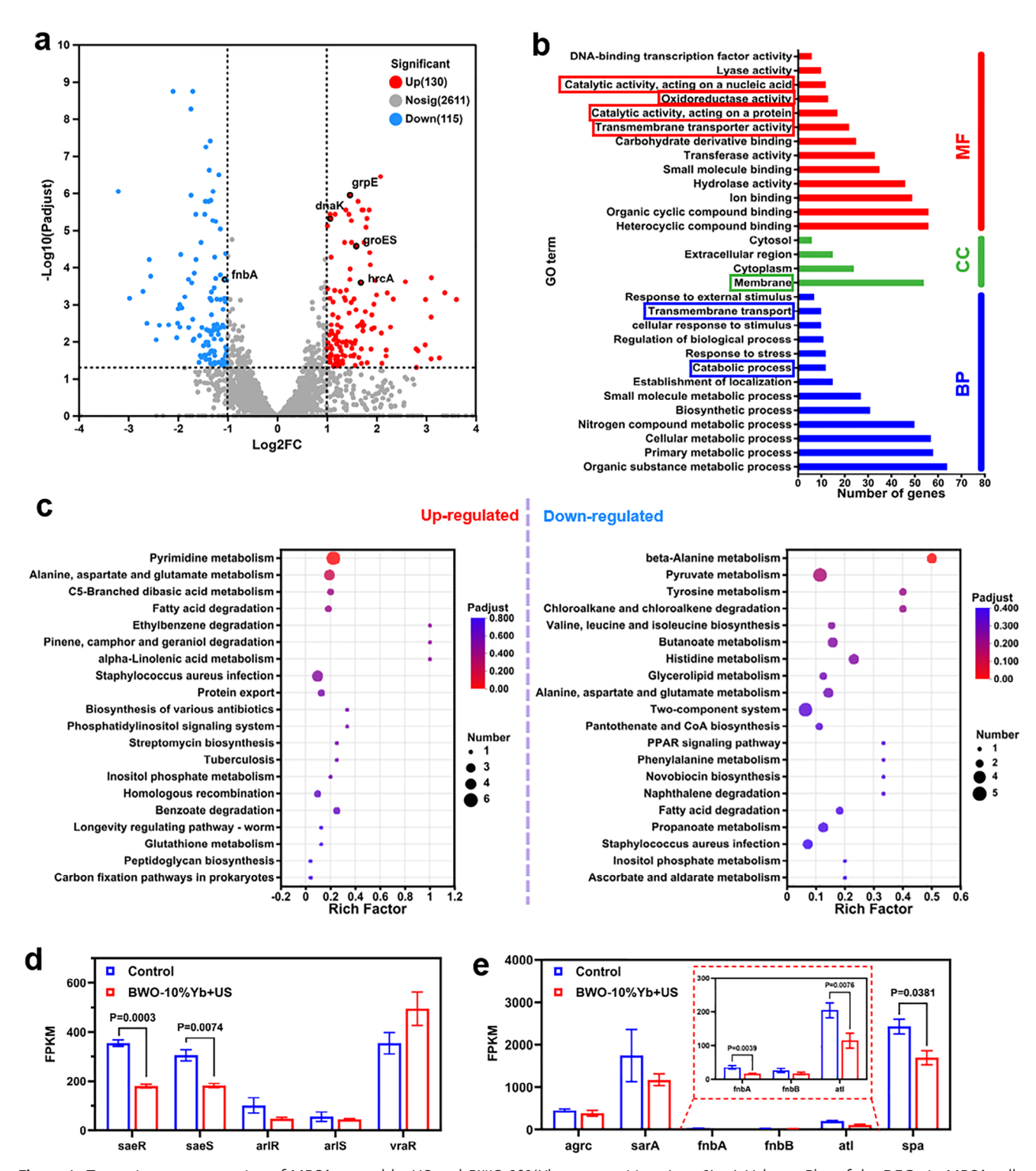


**Figure 4.** Transcriptome sequencing of MRSA treated by US and BWO-10%Yb sonosensitizer (n = 3). a) Volcano Plot of the DEGs in MRSA cells. b) Gene ontology (GO) term classification analysis based on the DGEs. c) The KEGG pathways enriched by the up-regulated and down-regulated DEGs. The Fragments per kilobase million (FPKM) genes associated with d) TCS pathway and e) biofilm formation.



www.afm-journal.de

enriched in pyruvate metabolism, glycerolipid metabolism, and two-component system (TCS) pathways. Notably, TCS is an essential signaling mechanism in bacteria that helps them adapt to environmental changes. The Fragments per kilobase million (FPKM) and heatmap of genes associated with the TCS pathway are displayed in Figures 4d and S14 (Supporting Information). Genes like saeR and saeS were downregulated, which may suggesting efforts to maintain membrane integrity by removing toxic compounds. The downregulated TCS pathway can disrupt the adaptive responses of bacteria, making them more susceptible to oxidative stress and resulting in downregulated biofilm formation (Figure 4e).

# 2.5. Construction of BWO-10%Yb PVA Hydrogel Platform for In Vivo Applications

Although BWO-10%Yb NSs have shown great promise as a sonodynamic antibacterial sonosensitizer, the biocompatibility of inorganic nanostructures remains a significant challenge for further preclinical applications. Hence, before conducting in vivo sonodynamic antibacterial tests, the BWO-10%Yb NSs were incorporated into PVA hydrogel to enhance their biocompatibility. Integrating BWO-10%Yb NSs sonosensitizer with a hydrogel matrix provides a powerful and targeted approach to combating bacterial infections. This combination improves biocompatibility of the sonosensitizer, facilitates ROS generation efficacy by optimizing the spatial distribution of the sonosensitizer, and allows for localized treatment, ultimately improving the effectiveness and safety of the treatment. Figure 5a depicts the process of loading BWO-10%Yb NSs into PVA hydrogel, abbreviated as BWO-Yb/PVA hydrogel. The concentration of BWO-10%Yb NSs used throughout the synthesis is 500 µg mL<sup>-1</sup> to ensure the capacity to generate sufficient ROS. Then the as-synthesized BWO-Yb/PVA hydrogel was placed into a mold before solidification to form a piece with a diameter of  $\approx 2$  cm (inset of Figure 5a). The in vitro cytotoxicity of BWO-10%Yb NSs and BWO-Yb/PVA hydrogel was assessed on RAW 246.7 macrophages and L929 fibroblasts using CCK-8 assay to evaluate the improvement in biocapacity. Given that the PVA hydrogel has the potential to absorb water from the cell culture medium, the hydrogel was immersed in the cell culture medium beforehand, and the leaching solution of the hydrogel was used to conduct the cell viability test. The results of the cell viability of BWO-10%Yb NSs with increasing concentration and leaching solution of the hydrogel are displayed in Figure 5b,c. Compared with the control groups, the cell viability of RAW cells and L929 fibroblasts incubated with BWO-10%Yb NSs declined significantly with the increase of BWO-10%Yb NSs concentration. The viability of RAW cells and L929 fibroblasts decreased to  $\approx$ 25% and  $\approx$ 50%, respectively, when exposed to a concentration of 500 µg mL<sup>-1</sup> BWO-10%Yb NSs, suggesting that BWO-10%Yb NSs exhibit significant cytotoxicity. In comparison, after 24 h of incubation with the PVA and BWO-Yb/PVA hydrogel leaching solution, the RAW cells and L929 fibroblasts showed no significant change compared to the blank group. Therefore, the as-synthesized BWO-Yb/PVA hydrogel platform effectively enhanced the biocompatibility of BWO-10%Yb NSs and provided the possibility for in vivo sonodynamic antibacterial applications.

To ensure a satisfactory loading of BWO-10%Yb NSs in PVA hydrogel, the structure of BWO-Yb/PVA hydrogel was further evaluated with SEM. To investigate the cross section of the PVA and BWO-Yb/PVA hydrogel, the hydrogels were freeze-dried and then fractured in liquid nitrogen. The SEM image in Figure 5d illustrates the porous structure of the cross section in BWO-Yb/PVA hydrogel. In addition, the SEM and EDX mapping of BWO-Yb/PVA hydrogel in Figure 5e further indicates the element distribution of C, O, Bi, and W, revealing the effective integration of BWO-10%Yb NSs into the PVA hydrogel.

The sonodynamic antibacterial capability of BWO-Yb/PVA hydrogel is also evaluated using a plate counting analysis. The suspensions of MRSA after different treatments (Control US(-), Control US(+), BWO-10%Yb US(-), BWO-10%Yb US(+), BWO-Yb/PVA US(-), BWO-Yb/PVA US(+)) were continuously diluted from 10<sup>6</sup> to 10<sup>2</sup> CFU mL<sup>-1</sup> and 10 µL of each diluent was dropped on an LB agar plate and cultured at 37 °C for 20 h. As shown in Figure 5f, there is no significant difference in the colonies between the groups treated without US irradiation and the USonly group. The quantitative analysis of the bacteria colonies in Figure 5f is exhibited in Figure 5g. A 100% reduction in MRSA (p = 0.0037) was seen after being treated with BWO-10%Yb NSs and US (BWO-10%Yb NSs US (+)), whereas the concentration of MRSA treated by BWO-Yb/PVA and US (B-PVA US (+)) is two orders of magnitude lower (p = 0.0031). Therefore, although the sonodynamic antibacterial capability of BWO-Yb/PVA hydrogel is inferior to bare BWO-10%Yb NSs, it still demonstrates considerable potential for in vivo sonodynamic antibacterial applications. Moreover, the tensile and compressive characteristics of two hydrogels were further evaluated by stress-strain curves (Figure \$15, Supporting Information). The BWO-Yb/PVA hydrogel exhibited superior tensile strength and stiffness, particularly in medium to high strain areas, along with enhanced toughness. In addition, BWO-Yb/PVA hydrogel also has excellent compressive resistance across a range of strains, offering enhanced stability in protecting the wound site. The superior mechanical and bactericidal capabilities of the BWO-Yb/PVA hydrogel render it appropriate for application in in vivo bacterial-infected wound sites.

#### 2.6. In Vivo Sonodynamic Wound Healing Therapy

Building upon the impressive antibacterial efficacy of the in vitro BWO-10%Yb NSs-mediated SDT, the antibacterial effect in vivo was further assessed. The animal test was performed under the approval of Animal Subjects Ethic Sub-committee (ASESC) of the Hong Kong Polytechnic University (Ref No. ARSA-24141-CRF-AP). All procedures adhered to the existing ethical guidelines stipulated by the ASESC at The Hong Kong Polytechnic University. All the animal tests involving bacteria were performed in an Animal Biosafety Level 2 (ABSL-2) laboratory. A wound infection model was created on the back of the 6-week-old BALB/C mouse by making a 6 mm diameter incision and applying a suspension of MRSA (1  $\times$  10<sup>8</sup> CFU mL<sup>-1</sup>, 25  $\mu$ L) to the wound area. The wound area was then tightly wrapped with a bandage for 24 h to ensure infection before the treatments. Afterward, the mice were randomly separated into 5 groups (n = 6) for different treatments, i.e., Control US(+), PVA US(+), BWO-Yb/PVA

16163028, 0, Downloaded from https://advanced.onlinelibrary.wiley.com/doi/10.1002/adfm.202511512 by HONG KONG POLYTECHNIC UNIVERSITY HU NG HOM, Wiley Online Library on [2609/2025]. See the Terms and Conditions (https://onlinelibrary.wiley.com/term/

and-conditions) on Wiley Online Library for rules of use; OA articles are governed by the applicable Creative Commons License

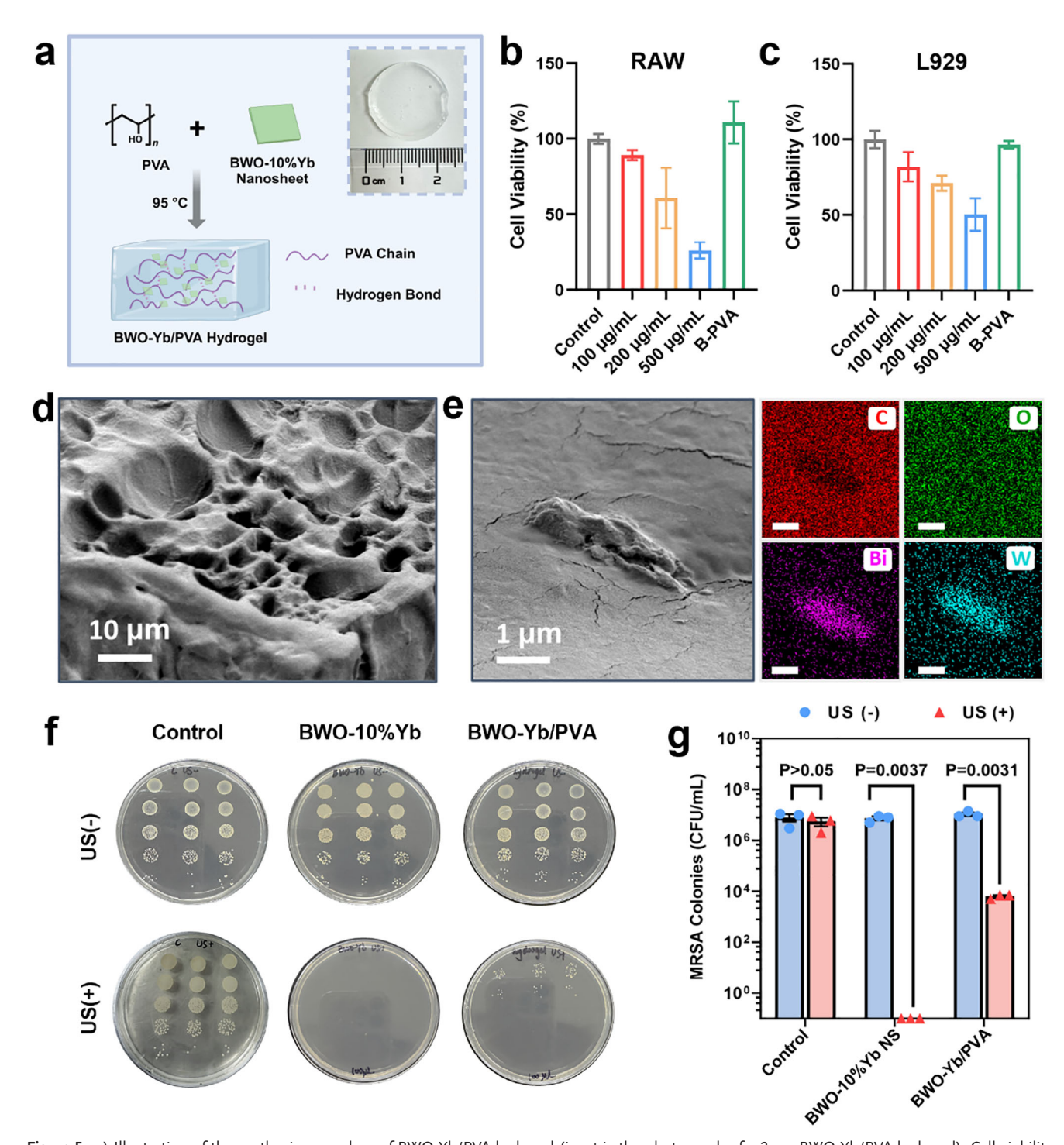


Figure 5. a) Illustration of the synthesis procedure of BWO-Yb/PVA hydrogel (inset is the photograph of a 2 cm BWO-Yb/PVA hydrogel). Cell viability of BWO-10%Yb NSs and BWO-Yb/PVA hydrogel leaching solution toward b) RAW 246.7 macrophages and c) L929 fibroblasts. d) SEM image of the cross section of BWO-Yb/PVA hydrogel. e) SEM and EDS mapping images of BWO-Yb/PVA hydrogel, indicating element distribution of C, O, Bi, W. Scale bar:  $1 \, \mu m$ . f) Photograph of MRSA colonies after different treatments with continuous dilution ratio coating on the LB agar plate. g) Corresponding MRSA-killing abilities of BWO-10%Yb NSs and BWO-Yb/PVA hydrogel. The error bars indicate mean  $\pm$  SEM. The statistical analysis was performed using an unpaired t-test.



US(-) groups were much higher, suggesting that the inflammatory response caused by MRSA infection was evident in these groups. As for the MCV and MPV, the result in the other four groups is much higher than that of the BWO-Yb/PVA US(+) group, indicating that the mice in the other groups still have a blood clotting process. [46] Meanwhile, the WBCs and neutrophils in the PVA US(+) group are lower than the standard range. The red blood cells (RBC) and the blood platelet count (PLT) of the mice in each group are almost equal (Figure S17, Supporting information).

US(-), and BWO-Yb/PVA US(+). The US irradiation power is 1.5 W cm<sup>-2</sup>, 50% duty cycle, 1 MHz, and the treatment duration is 5 min. Given the viscosity and stretchability of PVA hydrogel. it can directly adhere to the back of the mice in the hydrogel treatment group to cover the wound region without any binding agent (Figure \$16, Supporting Information). A schematic illustration of the MRSA-infected wound healing model and the treatment process is depicted in Figure 6a. The body weight (Figure 6b) and wound closure of the mice in each group were monitored every two days after the therapy to evaluate the wound healing progress. As shown in Figure 6c, the wound healing rates were comparable across the control (Control US(-)), US only (Control US (+)), and PVA US (+) groups. The wound sites of the mice in these three groups exhibited continuous festering from Day 1 to Day 10, indicating a severe infection of MRSA and inflammation in the wound area. The wound treated with BWO-Yb/PVA hydrogel but not exposed to the US showed a slightly accelerated woundhealing process. Nevertheless, the mice that received treatment with BWO-Yb/PVA hydrogel along with US irradiation demonstrated prevention of bacterial infection and a notable speed-up in scabbing. The relative wound area (%) was calculated by the following equation according to the photograph using ImageJ.

Relative Wound Area (%) = (Area (Day 1) - Area (Day 10)) /(Area (Day 1))  $\times$  100% (1)

According to the statistical analysis of the wound area measurements (Figure 6d), the wound area of the mice in the BWO-Yb/PVA US (+) group on day 10 decreased to only 25% of the initially infected wound area on Day 1 (p = 0.032). In contrast, the mice in other groups demonstrated no significant difference compared to the Control US(-) group (p > 0.05). Notably, the wound area of the mice in the Control US(+) group was more severe than that of the control group throughout the healing process, which may be associated with the mechanical damage caused by US without the protection of the hydrogel. The body weight of the mice is also consistent with the wound-healing process. Figure 6b reveals that the body weight of the mice in all groups showed a declining tendency in the early infection stage (Day 0-Day 2) and a constant increase from Day 2 to Day 10, except for the group exposed to US only. The US only group showed an apparent rise until Day 8, which might be attributed to severe bacterial infection and inflammation.

The mice were sacrificed on the 10<sup>th</sup> day after the therapy, then the blood was collected, and the wound region was dissected for further evaluation. Due to the fact that the bacterial infection always triggers an inflammatory response in the host, the inflammation in the infection models was assessed using standard blood examination, in which white blood cells and neutrophils are often used as inflammation indicators to screen for the severity of bacterial infection. In addition, red blood cells and blood platelets also act as indicators of the wound healing process. The results of standard blood examination of white blood cells (WBC), neutrophils (NEU), mean corpuscular volume (MCV), and mean platelet volume (MPV) are displayed in Figure 6e (the normal range is indicated by dashed rectangular lines). Compared with the BWO-Yb/PVA US(+) group, the numbers of WBCs and neutrophils in the Control US(-), Control US(+), and BWO-Yb/PVA

The dermal tissues around the wound area were dissected on Day 10 after the sacrifice for staining analysis. From the hematoxylin and eosin (H&E) staining in Figures 6f and S18 (Supporting Information), the dermal tissues in the four control groups showed more vascular dilatation, congestion, and bleeding, with more inflammatory cell infiltration. The BWO-Yb/PVA US(+) group showed no subcutaneous tissue defect and a reduced level of inflammatory cell infiltration compared to the other groups. The major organs, i.e., heart, liver, spleen, lung, and kidney of the mice in each group, were also collected and weighed to evaluate the impact of the US irradiation and bacterial infection. The H&E staining images and the weight of the organs are shown in Figures \$19,\$20 (Supporting Information), which demonstrate that the bacterial infection did not influence the organ weights and histological structure of the major organs throughout the wound healing duration. The Masson trichrome staining was conducted to assess the collagen accumulation in the wound area (Figure 6f; Figure S18, Supporting Information). All four control groups had necrotic scab tissues, and the epidermis of the wound region did not completely regenerate, with the regenerated collagen fibers poorly formed and loosely organized. Compared to the control groups, the BWO-Yb/PVA US(+) group exhibited a dense arrangement of new collagen fibers, indicating the satisfactory healing of the treated wound region. In addition, Gram staining was employed to further evaluate the remaining bacteria in the wound region on Day 10. As shown in Figure 6g, the skin of the mice in other treatment groups exhibited a considerable amount of dark purple patches (yellow dotted circle in Figure 6g), indicating that remnants of MRSA still existed in the wound area until Day 10. Conversely, the group treated with BWO-Yb/PVA hydrogel and US had negligible spots. These findings provided conclusive evidence that SDT treatment based on BWO-Yb/PVA hydrogel platform could generate ROS and induce oxidative stress that leads to bacterial death inside the wound, resulting in speed up the healing process in an MRSA-infected wound model.

# 3. Conclusion

In this work, we present a novel lanthanide-doped Bi<sub>2</sub>WO<sub>6</sub> NSs as sonosensitizers with high ROS generation performance for US-triggered enhanced sonodynamic antibacterial application. The doping of Yb ions in Bi<sub>2</sub>WO<sub>6</sub> NSs narrowed the band gap of Bi<sub>2</sub>WO<sub>6</sub> NSs and enhanced the H<sub>2</sub>O absorption, thereby facilitating improved ROS generation. Specifically, the Bi<sub>2</sub>WO<sub>6</sub> NSs with 10% of Yb doping concentration significantly improved the quantity of ROS generated under the trigger of US and present excellent in vitro inhibition rates against both gram-negative and gram-positive bacteria, indicating the capability of broad-spectrum bacteria elimination. Furthermore, the

16163028, 0, Downloaded from https://advanced.onlinelibrary.wiley.com/doi/10.1002/adfm.202511512 by HONG KONG POLYTECHNIC UNIVERSITY HUNG HOM, Wiley Online Library on [2609/2025]. See the Terms and Conditions (https://onlinelibrary.wiley.com/doi/10.1002/adfm.202511512 by HONG KONG POLYTECHNIC UNIVERSITY HUNG HOM, Wiley Online Library on [2609/2025]. See the Terms and Conditions (https://onlinelibrary.wiley.com/doi/10.1002/adfm.202511512 by HONG KONG POLYTECHNIC UNIVERSITY HUNG HOM, Wiley Online Library on [2609/2025]. See the Terms and Conditions (https://onlinelibrary.wiley.com/doi/10.1002/adfm.202511512 by HONG KONG POLYTECHNIC UNIVERSITY HUNG HOM, Wiley Online Library on [2609/2025]. See the Terms and Conditions (https://onlinelibrary.wiley.com/doi/10.1002/adfm.202511512 by HONG KONG POLYTECHNIC UNIVERSITY HUNG HOM, Wiley Online Library on [2609/2025]. See the Terms and Conditions (https://onlinelibrary.wiley.com/doi/10.1002/adfm.202511512 by HONG KONG POLYTECHNIC UNIVERSITY HUNG HOM, Wiley Online Library on [2609/2025]. See the Terms and Conditions (https://onlinelibrary.wiley.com/doi/10.1002/adfm.202511512 by HONG KONG POLYTECHNIC UNIVERSITY HUNG HOM, Wiley Online Library on [2609/2025]. See the Terms and Conditions (https://onlinelibrary.wiley.com/doi/10.1002/adfm.202511512 by HONG KONG POLYTECHNIC UNIVERSITY HUNG HOM.

onditions) on Wiley Online Library for rules of use; OA articles are governed by the applicable Creative Commons License

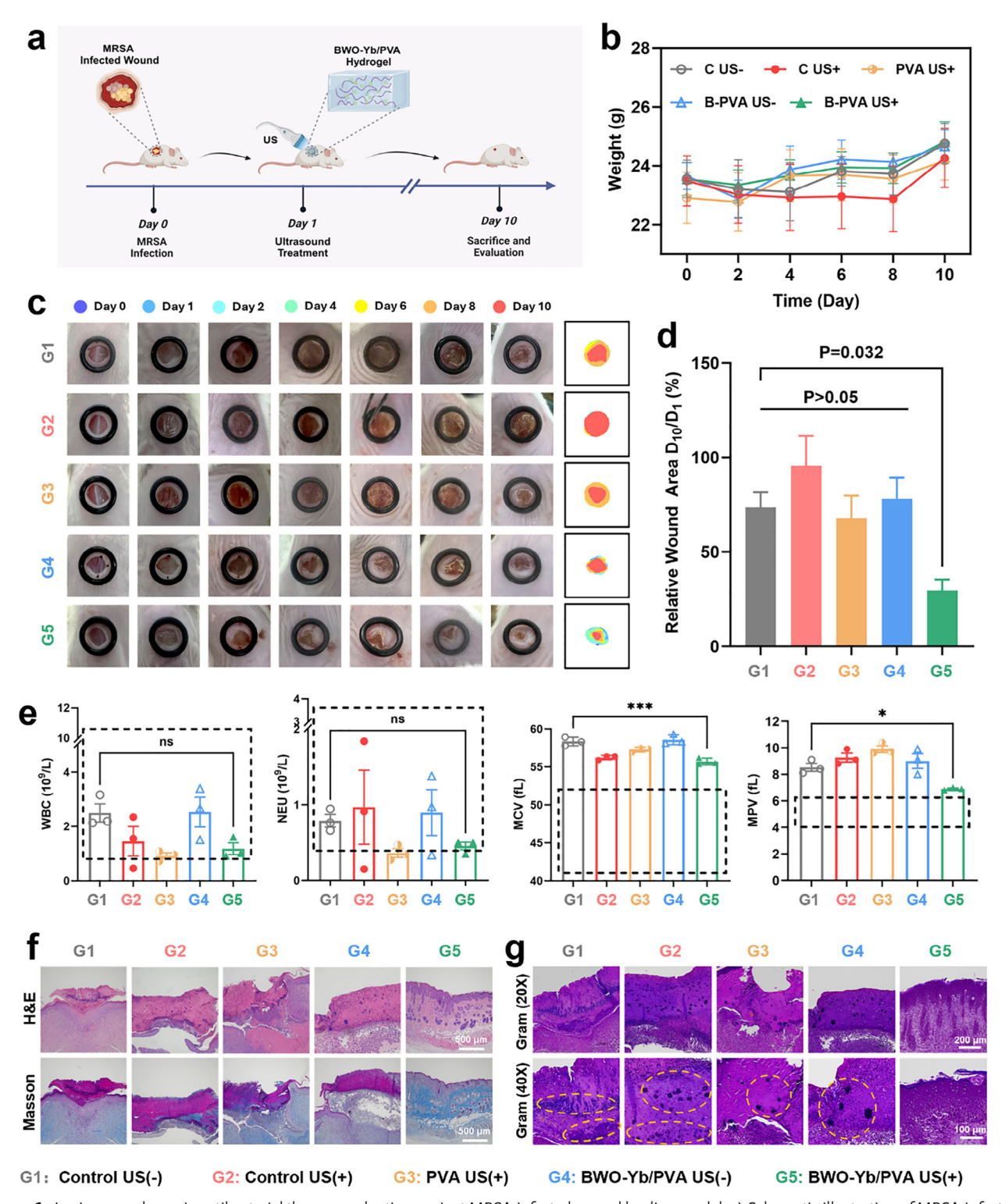


Figure 6. In vivo sonodynamic antibacterial therapy evaluation against MRSA-infected wound healing model. a) Schematic illustration of MRSA-infected wound healing model and the treatment process. b) Body weight changes of mice in different treatment groups. c) Representative photographs of the infected wound area from Day 0 to Day 10 in each group. The last column is the skeleton map depicting the changes in the wound area. d) Relative wound area (Day10/Day1) of the different groups. e) WBC, NEU, MCV, and MPV in the blood of MRSA-infected mice after 10 days of treatment. The error bars indicate mean  $\pm$  SEM. The statistical analysis was performed using one-way ANOVA with Dunnett's multiple-comparisons test: \*p < 0.05, \*\*p < 0.01, \*\*\*p < 0.001, and \*\*\*\*p < 0.0001; ns: not significant (p > 0.05). f) H&E (first row) and Masson (second row) staining images of the infected wound area after 10 days of treatment. Scale bars: 500 μm. g) Gram staining images of the infected wound area after 10 days of treatment of the MRSA cells, scale bars: 100 μm.

16163028, 0, Downloaded from https://advanced.onlinelibrary.wiley.com/doi/10.1002/adfm.202511512 by HONG KONG POLYTECHNIC UNIVERSITY HU NG HOM, Wiley Online Library on [2609/2025]. See the Terms and Conditions (https://onlinelibrary.wiley.com/terms-

and-conditions) on Wiley Online Library for rules of use; OA articles are governed by the applicable Creative Commons License

mechanism of sonodynamic antibacterial was deeply investigated at the transcriptome level. Then we construct a sonosensitizer-hydrogel platform to improve the biocompatibility of the inorganic sonosensitizer for in vivo SDT. The integration of sonosensitizer with hydrogel matrix is a strategic approach to enhance the biocompatibility of the sonosensitizer while ensuring efficient ultrasound-activated ROS generation by optimizing the spatial distribution of the sonosensitizer. In addition, the hydrogel matrix could adhere to specific infection sites and concentrate the sonosensitizer where it is most needed. This localized treatment minimizes systemic exposure and potential side effects, enhancing the safety profile of the therapy. The BWO-Yb/PVA hydrogel platform was applied to the MRSAinfected wound and significantly accelerated the wound healing process under US irradiation, with the wound area reduced by 75% in 10 days. Therefore, the findings of this study indicate the potential of 2D bismuth materials as innovative sonosensitizers. In addition, the biocompatible sonosensitizer-hydrogel platform further expands the application of 2D bismuth materials for in vivo SDT. Consequently, sonodynamic antibacterial therapy is more promising for addressing drug-resistant bacterial infections and potential deep-seated infections than light-activated photodynamic therapy, owing to the portable and low-cost US apparatus, adjustable US probe area, and deeper penetration of US. Although SDT is an emerging approach, there are still challenges and potential barriers to scaling this therapy for clinical use in human patients. For example, ensuring that sonosensitizer can be delivered effectively and safely to the target site in the human body is crucial for internal infection treatment. This involves surface modification of sonosensitizers with safe and stable targeting ligands. Moreover, determining the optimal ultrasound frequency, intensity, and duration is necessary to maximize efficacy while minimizing side effects in human tissue. Future research should focus on optimizing the ultrasound parameters for deep-seated infections and improving the targeting impact, which is necessary for translating this technology into clinical settings with the collaboration between researchers and clinicians.

### **Supporting Information**

Supporting Information is available from the Wiley Online Library or from the author.

## Acknowledgements

This work was supported by grants from the Research Grants Council of the Hong Kong Special Administrative Region, China (Project No. CRF No. C5110-20G and PolyU SRFS2122-5S02), and PolyU Grants (1-CE0H, 1-W30M, 1-W327, and 1-CD7V).

#### **Conflict of Interest**

The authors declare no conflict of interest.

# **Data Availability Statement**

The data that support the findings of this study are available from the corresponding author upon reasonable request.

## **Keywords**

antibacterial, Bi<sub>2</sub>WO<sub>6</sub> nanosheets, sonodynamic therapy, wound healing

Received: May 8, 2025 Published online:

- [1] C.-A. D. Burnham, J. Leeds, P. Nordmann, J. O'Grady, J. Patel, Nat. Rev. Microbiol. 2017, 15, 697.
- C. J. L. Murray, K. S. Ikuta, F. Sharara, L. Swetschinski, G. R. Aguilar, A. Gray, C. Han, C. Bisignano, P. Rao, E. Wool, Lancet 2022, 399, 629.
- [3] S. L. Bronzwaer, O. Cars, U. Buchholz, S. Mölstad, W. Goettsch, I. K. Veldhuijzen, J. L. Kool, M. J. Sprenger, J. E. Degener, Emerg. Infect. Dis. 2002, 8, 278.
- [4] E. Tacconelli, F. Sifakis, S. Harbarth, R. Schrijver, M. van Mourik, A. Voss, M. Sharland, N. B. Rajendran, J. Rodríguez-Baño, J. Bielicki, Lancet Infect. Dis. 2018, 18, 99.
- [5] D. Sun, X. Pang, Y. Cheng, J. Ming, S. Xiang, C. Zhang, P. Lv, C. Chu, X. Chen, G. Liu, N. Zheng, ACS Nano 2020, 14, 2063.
- [6] P.-Y. Xu, R. Kumar Kankala, S.-B. Wang, A.-Z. Chen, Ultrason. Sonochem. 2023, 100, 106617.
- [7] K. Su, L. Tan, X. Liu, Z. Cui, Y. Zheng, B. Li, Y. Han, Z. Li, S. Zhu, Y. Liang, X. Feng, X. Wang, S. Wu, ACS Nano 2020, 14, 2077.
- [8] Y. Hong, J. Zeng, X. Wang, K. Drlica, X. Zhao, Proc. Natl. Acad. Sci. USA 2019, 116, 10064.
- [9] B. Yang, Y. Chen, J. Shi, Chem. Rev. 2019, 119, 4881.
- [10] R. Wang, Q. Liu, A. Gao, N. Tang, Q. Zhang, A. Zhang, D. Cui, Nanoscale 2022, 14, 12999.
- [11] H. Yang, L. Tu, J. Li, S. Bai, Z. Hu, P. Yin, H. Lin, Q. Yu, H. Zhu, Y. Sun, Coord. Chem. Rev. 2022, 453, 214333.
- [12] W. Li, Y. Song, X. Liang, Y. Zhou, M. Xu, Q. Lu, X. Wang, N. Li, Biomaterials 2021, 276, 121063.
- [13] D. Li, Y. Yang, D. Li, J. Pan, C. Chu, G. Liu, Small 2021, 17, 2101976.
- [14] X. Xing, S. Zhao, T. Xu, L. Huang, Y. Zhang, M. Lan, C. Lin, X. Zheng, P. Wang, Coord. Chem. Rev. 2021, 445, 214087.
- [15] X. Cao, M. Li, Q. Liu, J. Zhao, X. Lu, J. Wang, Small 2023, 19, 2303195.
- [16] Y. Wang, Y. Sun, S. Liu, L. Zhi, X. Wang, Ultrason. Sonochem. 2020, 63,
- [17] D. He, W. Wang, N. Feng, Z. Zhang, D. Zhou, J. Zhang, H. Luo, Y. Li, X. Chen, J. Wu, ACS Appl. Mater. Interfaces 2023, 15, 15140.
- [18] Y. Guo, C. Mao, S. Wu, C. Wang, Y. Zheng, X. Liu, Small 2024, 20, 2400732.
- [19] L. Pan, S. Sun, Y. Chen, P. Wang, J. Wang, X. Zhang, J.-J. Zou, Z. L. Wang, Adv. Energy Mater. 2020, 10, 2000214.
- [20] Y. Zhao, T. Huang, X. Zhang, Y. Cui, L. Zhang, L. Li, Z. L. Wang, BMEMat 2023, 1, 12006.
- [21] S. Chen, P. Zhu, L. Mao, W. Wu, H. Lin, D. Xu, X. Lu, J. Shi, Adv. Mater. 2023, 35, 2208256.
- [22] W. Qin, Q. Yang, C. Zhu, R. Jiao, X. Lin, C. Fang, J. Guo, K. Zhang,
- Small 2024, 20, 2311228. [23] S. Liang, X. Deng, G. Xu, X. Xiao, M. Wang, X. Guo, P. A. Ma, Z. Cheng,
- D. Zhang, J. Lin, Adv. Funct. Mater. 2020, 30, 1908598. [24] F. Gao, G. He, H. Yin, J. Chen, Y. Liu, C. Lan, S. Zhang, B. Yang,
- Nanoscale 2019, 11, 2374.
- [25] C. Dai, S. Zhang, Z. Liu, R. Wu, Y. Chen, ACS Nano 2017, 11, 9467.
- [26] C. Mao, W. Jin, Y. Xiang, Y. Zhu, J. Wu, X. Liu, S. Wu, Y. Zheng, K. M. C. Cheung, K. W. K. Yeung, Adv. Mater. 2023, 35, 2208681.
- [27] S. Tu, H. Huang, T. Zhang, Y. Zhang, Appl. Catal., B 2017, 219, 550.
- [28] Y. Dong, S. Dong, B. Liu, C. Yu, J. Liu, D. Yang, P. Yang, J. Lin, Adv. Mater. 2021, 33, 2106838.
- [29] Z. Yang, Y. Luo, H. Yu, K. Liang, M. Wang, Q. Wang, B. Yin, H. Chen, Adv. Mater. 2022, 34, 2108908.

16163028, 0, Downloaded from https://advanced.onlinelibrary.wiley.com/doi/10.1002/adfm.202511512 by HONG KONG POL YTECHNIC UNIVERSITY HU NG HOM, Wiley Online Library on [26/09/2025]

. See the Terms

and-conditions) on Wiley Online Library for rules of use; OA articles are governed by the applicable Creative Commons License



www.advancedsciencenews.com

- [30] L. Wei, Y. Chen, X. Yu, Y. Yan, H. Liu, X. Cui, X. Liu, X. Yang, J. Meng, S. Yang, L. Wang, X. Yang, R. Chen, Y. Cheng, ACS Appl. Mater. Interfaces 2022. 14. 53491.
- [31] H. Djani, P. Hermet, P. Ghosez, J. Phys. Chem. C 2014, 118, 13514.
- [32] M. Maczka, W. Paraguassu, A. G. S. Filho, P. T. C. Freire, J. M. Filho, J. Hanuza, *Phys. Rev. B* **2008**, *77*, 094137.
- [33] X. Zhong, X. Wang, L. Cheng, Y. A. Tang, G. Zhan, F. Gong, R. Zhang, J. Hu, Z. Liu, X. Yang, Adv. Funct. Mater. 2020, 30, 1907954
- [34] Y. Song, W. Li, H. Jing, X. Liang, Y. Zhou, N. Li, S. Feng, Chem. Eng. J. 2022, 438, 135558.
- [35] X. Xiao, Y. Zhao, P. A. Ma, Z. Cheng, J. Lin, Chem. Eng. J. 2022, 440, 135812.
- [36] S. Li, S. Dong, W. Xu, S. Tu, L. Yan, C. Zhao, J. Ding, X. Chen, Adv. Sci. 2018, 5, 1700527.
- [37] B. Jia, G. Li, E. Cao, J. Luo, X. Zhao, H. Huang, Mater. Today Bio 2023, 19, 100582.

- [38] Y. Zhou, Y. Zhang, M. Lin, J. Long, Z. Zhang, H. Lin, J. C. S. Wu, X. Wang, Nat. Commun. 2015, 6, 8340.
- [39] H. Gunduz, S. Kolemen, E. U. Akkaya, Coord. Chem. Rev. 2021, 429, 213641.
- [40] Y. Ding, Y. Zhao, S. Yao, S. Wang, X. Wan, Q. Hu, L. Li, Small 2023, 19, 2300327.
- [41] R. Yang, F. Cheng, Y. Zhao, S. Ye, ACS Appl. Mater. Interfaces 2020, 12, 44961.
- [42] M. Li, D. Yang, X. Huang, H. Zhang, Y. Zhao, B. Yin, Q. Pan, J. Kang, N. Zheng, X. Liu, J. Qiu, Z. Yang, G. Dong, Adv. Mater. 2022, 34, 2201413.
- [43] N. Kwon, H. Weng, M. A. Rajora, G. Zheng, Angew. Chem., Int. Ed. 2025, 64, 202423348.
- [44] S. Zhao, J. W. Adamiak, V. Bonifay, J. Mehla, H. I. Zgurskaya, D. S. Tan, Nat. Chem. Biol. 2020, 16, 1293.
- [45] Y. Liu, C. Huang, W. Yue, X. Wang, Y. Sun, W. Bi, L. Wang, Y. Xu, Carbon 2024, 224, 119085.
- [46] U. D. S. Sekhon, A. S. Gupta, ACS Biomater. Sci. Eng. 2018, 4, 1176.